

Methods

High mass resolution, spatial metabolite mapping enhances the current plant gene and pathway discovery toolbox

Yonghui Dong¹ , Prashant Sonawane¹ , Hagai Cohen¹, Guy Polturak¹ , Liron Feldberg² , Shelly Hen Avivi¹, Ilana Rogachev¹ and Asaph Aharoni¹ 

¹Department of Plant Sciences, Weizmann Institute of Science, Rehovot 761001, Israel; ²Department of Analytical Chemistry, Israel Institute for Biological Research, Ness Ziona 7410001, Israel

Summary

Author for correspondence:

Asaph Aharoni

Tel: +97289346343

Email: asaph.aharoni@weizmann.ac.il

Received: 9 April 2020

Accepted: 6 July 2020

New Phytologist (2020) **228**: 1986–2002
doi: 10.1111/nph.16809

Key words: gene function, MALDI (matrix-assisted laser desorption/ionisation), mass spectrometry imaging (MSI), secondary metabolites, spatial distribution.

- Understanding when and where metabolites accumulate provides important cues to the gene function. Mass spectrometry imaging (MSI) enables *in situ* temporal and spatial measurement of a large assortment of metabolites, providing mapping information regarding their cellular distribution.
- To describe the current state and technical advances using MSI in plant sciences, we employed MSI to demonstrate its significant contribution to the study of plant specialised metabolism.
- We show that coupling MSI with: (1) RNA interference (RNAi), (2) virus induced gene silencing (VIGS), (3) agroinfiltration or (4) samples derived from plant natural variation provides great opportunities to understand the accurate gene–metabolite relationship and discover novel gene-associated metabolites. This was exemplified in three plant species (i.e. tomato, tobacco and wheat) by mapping the distribution of metabolites possessing a range of polarities. In particular, we demonstrated that MSI is able to spatially map an entire metabolic pathway, including intermediates and final products, in the intricate biosynthetic route to tomato fruit steroidal glycoalkaloids.
- We therefore envisage MSI as a key component of the metabolome analysis arsenal employed in plant gene discovery strategies.

Introduction

Given the ever-increasing numbers of plant species whose full genomes have been sequenced, there is a growing demand for gene functional annotation (Tohge & Fernie, 2010). Typically, only 50% or less of the genes in a newly reported genome can be assigned to some extent using homology searching (Ossipov *et al.*, 2007; Putri *et al.*, 2013). Monitoring metabolites is crucial for assigning gene function; while mRNAs and proteins are viewed as media in the flow of gene expression, metabolites are the end products and directly reflect changes in phenotype and function (Putri *et al.*, 2013). Metabolomics has been applied widely to link phenotypes to genotypes in diverse biological systems (Ossipov *et al.*, 2007; Matsuda *et al.*, 2012; Zampieri & Sauer, 2017), and has evolved as an important functional genomics tool (Bino *et al.*, 2004; Saito & Matsuda, 2010; Putri *et al.*, 2013). This technology exhibits several key limitations including the intricacy of data acquisition at cell type and subcellular levels. This links tightly to a second constraint of metabolomics, namely obtaining wide metabolome coverage when analysing minute amounts of a specific sample.

Plants are highly differentiated multicellular organisms that consist of multiple specialised organs and tissues with unique anatomical features; anatomical differentiation often parallels differential gene expression and metabolite profiles (Saito & Matsuda, 2010; Zampieri & Sauer, 2017). As such, information on metabolite distribution has been regarded as an important read-out of tissue-level gene function (D. Li *et al.*, 2016).

Unfortunately, spatial information is usually lost in holistic metabolomics studies in which the analysis is performed on tissue or organ homogenates (Moussaieff *et al.*, 2013; Dong *et al.*, 2016a). Therefore, it is not surprising that spatially resolved metabolomics is increasingly recognised as an essential functional genomics tool. This approach offers at least two unique advantages: (1) it enables the detection of highly spatially localised metabolites that are typically undetectable due to sample dilution effect in bulk metabolomics analysis; and (2) it provides accurate tissue-specific, gene-to-metabolite correlation, from which significant clues regarding gene functions involved in the biosynthesis of related metabolites could be obtained (Sumner *et al.*, 2015).

In recent years, mass spectrometry imaging (MSI) has emerged as one of the most effective tools for spatially resolved

metabolomics. It enables the determination of the mass-to-charge ratio (m/z), relative abundance and spatial distribution of a large assortment of molecules directly from the tissue section. During MSI analysis the tissue section is measured in a predefined raster, which generates a mass spectrum at each measurement point (i.e. pixel). The ion intensity for a specific m/z value is then extracted from each pixel and arranged into a heat map-like image, namely an MS image. In addition, the optical image of the sample can be co-registered with the MS image for precise visual inspection of the molecular distribution (Heyman & Dubery, 2016; Sturtevant *et al.*, 2016) (Fig. S1). Several ion sources have been used for MSI, among them matrix-assisted laser desorption/ionisation (MALDI), desorption electrospray ionisation (DESI) and secondary ion mass spectrometry (SIMS) are the three major examples (Horn & Chapman, 2014a; B. Li *et al.*, 2016). To date, MALDI has been the most widely used MSI technology (Palmer *et al.*, 2016).

Recently MSI has received considerable attention in plant research, and has demonstrated its potential in various applications such as plant physiology and development (Bhandari *et al.*, 2015; Sturtevant *et al.*, 2020), natural products identification (Horn *et al.*, 2013; Fu *et al.*, 2019), and plant–environment interactions (Costa *et al.*, 2019; Korenblum *et al.*, 2020). In this study, we demonstrated that MSI can be coupled with different reverse genetics approaches to elucidate gene function. Metabolite profiles of model and commercially relevant plant species, which were either silenced or harbour mutations in a specific gene of interest, were compared with those of control plants using MALDI imaging. Tomato (*Solanum lycopersicum*), *Nicotiana benthamiana* (*N. benthamiana*) and wheat (*Triticum aestivum*) lines that were genetically different due to either RNA interference (RNAi), virus induced gene silencing (VIGS), agroinfiltration or natural variation were used in this study. Parallel results acquired by liquid chromatography- or gas chromatography-mass spectrometry (LC-MS or GC-MS) of tissue homogenates were employed in these experiments. Finally, this work discusses the current limitations, advantages and opportunities of coupling MSI with reverse genetics approaches to infer the function of genes.

Materials and Methods

Plant material and gene manipulation

GAME25 silencing construct (RNAi, *GAME25i*) preparation and *Agrobacterium*-mediated tomato (cv Micro Tom) transformation were performed as described previously (Sonawane *et al.*, 2018). Green and red fruit from positive *GAME25*-silenced transgenic lines (selected by quantitative real time-PCR; qRT-PCR) were subjected to MALDI imaging and LC-MS analysis. For VIGS of *GAME31* in tomato (*Solanum lycopersicum*; cv Micro Tom) plants expressing *DELILA* (*Del*) and *ROSEA1* (*Ros1*) transcription factors under fruit-specific promoter E8 (*E8:Del/Ros1* MT) were grown in a climate-controlled glasshouse at 24°C : 18°C, day : night regime with natural light. The *GAME31* VIGS construct was generated by introducing a 298-bp *GAME31* fragment (Forward primer: GAATTCATGGATTGATGTGATTATTT CACC, Reverse primer: GAATTCCTTGAAAAGATCACT

TGGAGGAG) to pCR8/GW/TOPO (using *EcoRI* restriction enzyme) and further cloning to the pTRV2 binary vector using the Gateway LR Clonase II enzyme mix (Invitrogen). The VIGS experiment was performed on mature green-stage fruit (in which purple pigmentation started to accumulate), as described previously (Orzaez *et al.*, 2009) except that the final *Agrobacterium* optical density (OD₆₀₀) was 0.3. Tomato plants infected with *Agrobacterium*, containing the pTRV2 vector and harbouring only the *Del/Ros1* sequences were used as the control. Due to co-silencing of the desired gene (here *GAME31*) and *Del/Ros1* transcription factors, clear visible red sectors appeared on the background of purple fruit upon maturation. Silenced red patched fruit tissues were collected at 3- or 4-wk post infection and analysed for SGA profile by MALDI imaging and LC-MS. For agroinfiltration-mediated transient expression, *Nicotiana benthamiana* plants were grown in a climate room (22°C, 70% humidity; 18 h : 6 h, light : dark). Transient gene expression assays with the pDODA1, pAD1-GT, pYFP, pAD6 and pX11 vectors were performed as described previously (Polturak *et al.*, 2016, 2018). Leaf tissues used for MALDI imaging and LC-MS analysis were sampled 7 d post infiltration. Glaucous BL and the glossy CASL*2BS wheat lines were kindly provided by Moshe Feldman (Weizmann Institute of Science). They were grown in a glasshouse (22°C : 20°C, day : night). Flag leaf sheaths were used for MALDI imaging and GC-MS analysis.

MALDI imaging analysis

Sample preparation, MALDI imaging analysis and data processing were performed as described previously (Schleyer *et al.*, 2019; Korenblum *et al.*, 2020). Detailed MALDI imaging methods are provided in Supporting Information Methods S1. Three biological replicates were used for each study.

Scanning electron microscopy imaging

Cryo-scanning electron microscopy images of BL and CASL*2BS flag leaf sheath surfaces were obtained using a Jeol JSM-6360 LV scanning electron microscope (Tokyo, Japan) for ×500 magnification images. The sample preparation method was as described previously (Hen-Avivi *et al.*, 2016).

Liquid and gas chromatography-mass spectrometry (LC-MS/GC-MS)

Sample preparation and metabolic profiling of steroidal glycoalkaloids (SGAs), anthocyanins, betalains and epicuticular wax compounds in tomato fruit, *N. benthamiana* and wheat leaves were performed as described previously (Hen-Avivi *et al.*, 2016; Polturak *et al.*, 2016, 2018; Sonawane *et al.*, 2018). Detailed LC-MS and GC-MS methods are provided in Methods S1.

Data analysis

MALDI imaging raw data (.msi) were converted to the imzML format using FLEXIMAGING software (v.4.1, Bruker Daltonics,

Germany). The imzML files were then loaded to MATLAB-based software, MSiREADER (v.1.01) (Bokhart *et al.*, 2018), to extract the average peak intensity for relative quantification. LC-MS data were processed using the TARGETLYNX program (Waters, Milford, MA, USA), and the peak area was used for relative quantification. GC-MS data were processed using MSD CHEMSTATION software (Agilent), and the normalised peak area against the C₂₄ alkane internal standard signal was used for relative quantification. Extracted peak intensities from MALDI imaging and peak areas from LC-MS or GC-MS were saved in .csv format for further statistical analysis. Statistical analysis was performed using the open source software R (R Core Team, 2019). Differences between paired groups were tested for significance using the Wilcoxon's signed-rank test; differences among multiple groups were tested for significance using Kruskal–Wallis test. Bar charts were produced using the R package GGPLOT2 (Wickham, 2016), and the *y*-axis was square root transformed for better visualisation of extreme values. Clustering of samples was performed using principal component analysis (PCA) with R package GGFORTIFY (Tang *et al.*, 2016).

Results

Using ultra-high mass resolution MALDI imaging to trace the steroidal glycoalkaloids pathway in tomato fruit

Steroidal glycoalkaloids (SGAs) are nitrogen-containing specialised metabolites renowned for their production in Solanaceae species. They typically accumulate in different tissues, providing the plant with a constitutive chemical barrier against a broad range of pathogens and predators (Yamanaka *et al.*, 2009; Schwahn *et al.*, 2014; Sonawane *et al.*, 2018). The presence or absence of a double bond at the C-5,6 position (termed here unsaturated and saturated, respectively), determines a significant part of the large structural diversity among SGAs (Sonawane *et al.*, 2018). In tomato, α -tomatine (saturated) and dehydrotomatine (unsaturated) are the major SGAs accumulating in green fruit tissues. Once tomato fruit ripens and reaches the mature red ripe stage, α -tomatine and dehydrotomatine are converted into various saturated and unsaturated SGA derivatives, and ultimately to esculeosides and dehydroesculeosides, respectively (Itkin *et al.*, 2011) (Fig. 1).

In cultivated tomato fruit, unsaturated SGAs represent only 2.5–10% of their saturated counterparts (Sonawane *et al.*, 2018). The short-chain dehydrogenase/reductase GLYCOALKALOID METABOLISM25 (GAME25) has been recently reported to catalyse the committed step in the conversion of dehydrotomatidine (unsaturated) to tomatidine (saturated) in tomato fruit (Sonawane *et al.*, 2018). To further elucidate the role of GAME25 in SGA metabolism, we silenced *GAME25* in tomato plant using RNAi. *GAME25* transcript levels were found to be significantly reduced in *GAME25i* tomato fruits at both mature green and mature red ripe stages ($P < 0.05$) (Fig. S2). PCA of metabolic profiles also showed clear discrimination between *GAME25i* and wild-type (WT) tomato fruits at mature green and mature red ripe stages, respectively (Fig. S3). As α -tomatine

and dehydrotomatine are the major SGAs in green fruit, we first compared their distribution and abundance in wild-type and *GAME25i* green tomato fruits using MALDI imaging. Both metabolites were detected in wild-type and *GAME25i* tomato fruits, and they were distributed homogeneously across the fruit sections except that their abundances were relatively low in seeds (Fig. 2a). Although similar in spatial localisation, these SGAs vary significantly in their amounts: α -tomatine is abundant in wild-type while dehydrotomatine accumulated to a higher level in *GAME25i* fruit (Fig. 2a) (Yamanaka *et al.*, 2009). Unexpectedly, a severe decline in the mass measurement accuracy (MMA) of α -tomatine was observed in *GAME25i* tomato fruit; it was detected at m/z 1034.5446 with a mass accuracy of 8 ppm. By contrast, it was detected at m/z 1034.5533 in wild-type tomato fruit with a mass accuracy of -0.29 ppm. The degradation of MMA was clearly not due to instrument malfunction during data acquisition as the mass accuracies for α -tomatine in wild-type, and dehydrotomatine in wild-type and *GAME25i* tomato fruit were all within the accepted mass accuracy window (< 2 ppm). A careful examination of the MALDI imaging spectra showed that it was due to insufficient mass resolution (Fig. 2b). The ion peak m/z 1034.5446 detected in *GAME25i* appeared to be the unresolved α -tomatine peak (C₅₀H₈₄NO₂₁, [M+H]⁺, theoretical m/z 1034.5530) and mainly the second ¹³C isotope peak of dehydrotomatine (¹²C₄₈¹³C₂H₈₂NO₂₁, [M+H]⁺, theoretical m/z 1034.5441) (Fig. 2c). Apparently, the mass resolution of $R = 115\,000$ at m/z 400 used in our MALDI imaging experiment was insufficient to resolve the α -tomatine ion (m/z 1034.5530) and the second ¹³C isotope of dehydrotomatine ion (m/z 1034.5441). A minimum mass resolution of $c. R = 287\,500$ at m/z 400 was required to distinguish the two neighbouring peaks. Therefore, an ultra-high mass resolution MALDI imaging was performed with mass resolution being $R = 1\,400\,000$ at m/z 400. The two ions were well separated under the new instrument settings, with α -tomatine ion being detected at m/z 1034.5529 with a mass accuracy of -0.18 ppm in *GAME25i* fruit (Fig. 2e). Similarly, as shown in Fig. 2a, both metabolites were abundant in fruit epidermis and pericarp, but α -tomatine was higher in wild-type and dehydrotomatine higher in *GAME25i* fruit (Fig. 2d).

The major metabolic change in SGA composition during tomato fruit ripening is the conversion of the entire pool of α -tomatine to esculeosides, and dehydrotomatine to dehydroesculeosides by several 'decorating' reactions including hydroxylation, acetylation and glycosylation (Schwahn *et al.*, 2014). Next, we employed MALDI imaging to visualise and quantify SGAs composition in wild-type and *GAME25i* tomato fruits at the mature red ripe stage. The entire repertoire of saturated and unsaturated SGAs shown in Fig. 1 were identified using MALDI imaging and LC-MS analysis of tissue homogenates (Fig. 3; Tables S1, S2). The results showed that, upon silencing of the *GAME25* gene, levels of α -tomatine and its downstream saturated SGA derivatives were all significantly reduced compared with wild-type fruit. By contrast, levels of dehydrotomatine and its downstream unsaturated SGA derivatives were all increased in mature red ripe *GAME25i* fruit (Fig. 3b,c). In particular, MALDI images showed that saturated SGAs and

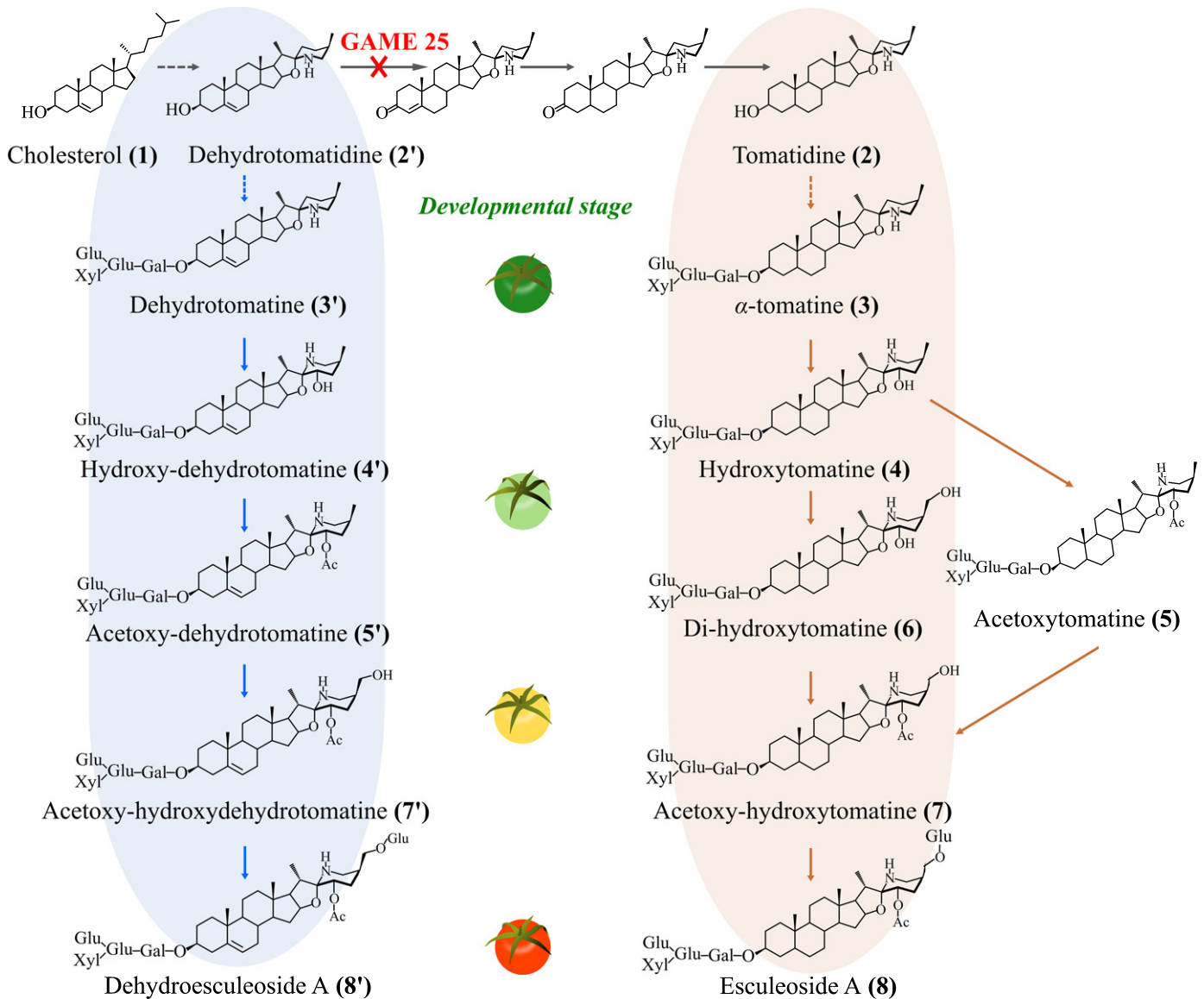
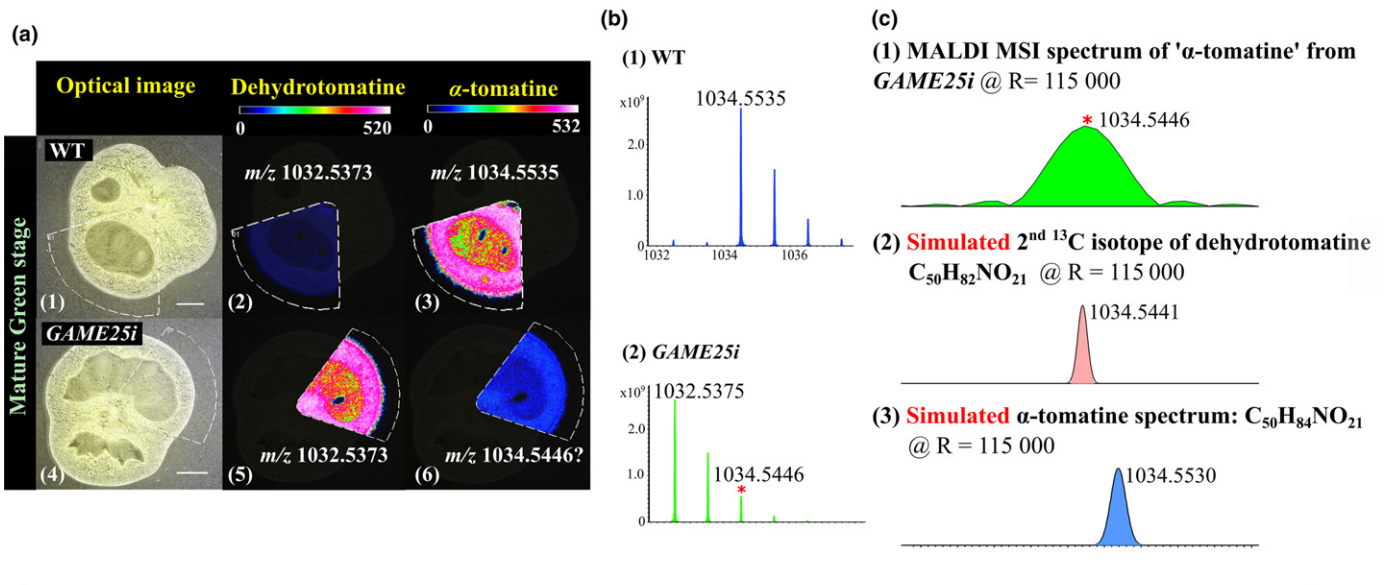


Fig. 1 Biosynthesis of steroidal glycoalkaloids (SGAs) during tomato fruit development. SGAs biosynthesis begins with the conversion of cholesterol (1) to unsaturated dehydrotomatidine (2'), which is the first steroidal alkaloid aglycone produced in green tomato fruit. Dehydrotomatidine is then converted to saturated tomatidine (2). Both dehydrotomatidine and tomatidine are glycosylated to form the predominant SGAs in green tomato fruit, namely, dehydrotomatine (3') and α -tomatine (3), respectively. Next, unsaturated and saturated hydroxy- and acetoxy-derivatives of α -tomatine (4–7) and dehydrotomatine (4'–7') start to accumulate at the breaker stage. In mature red ripe fruit, unsaturated and saturated esculeosides and lycopersides (8' and 8) are the most abundant SGAs. Silencing of the *GAME25* gene diverts the entire 'saturated' SGAs profile to the production of unsaturated SGAs. Dashed and solid arrows denote multiple and single enzymatic reactions in the pathway, respectively.

their respective unsaturated forms (e.g. esculeoside A and dehydroesculeoside A) exhibited very similar distribution patterns in wild-type and *GAME25i* fruit. During conversion of α -tomatine to esculeosides, and dehydrotomatine to dehydroesculeosides, saturated and unsaturated SGAs intermediates mostly accumulated in the epidermis layer of both wild-type and *GAME25i* fruit. Semiquantitative and distribution information together suggested that silencing of *GAME25* reroutes the entire saturated SGA repertoire towards the unsaturated SGAs branch, while the spatial distribution of saturated SGAs and their respective unsaturated forms remain the same in wild-type and *GAME25i* fruit (Fig. 3).

The capability to resolve isobaric species (molecules possessing the same nominal mass but different monoisotopic mass) using ultra-high mass resolution measurement offers several unique advantages to MSI. First, it increases the number of detected mass peaks; second, it improves confidence in molecular identification (Manicke *et al.*, 2010); third, it ensures more precise spatial distribution information as the isobaric ions may have different spatial distribution pattern (Feldberg *et al.*, 2018); and finally, it provides more accurate semiquantitative information. However, it is worth noting that ultra-high mass resolution MSI is not always the preferred choice as the amount of acquisition time is significantly increased. For instance, the overall analysis

High mass resolution MALDI Imaging, $R = 115\,000$ @ m/z 400



Ultra-high mass resolution MALDI Imaging, $R = 1400\,000$ @ m/z 400

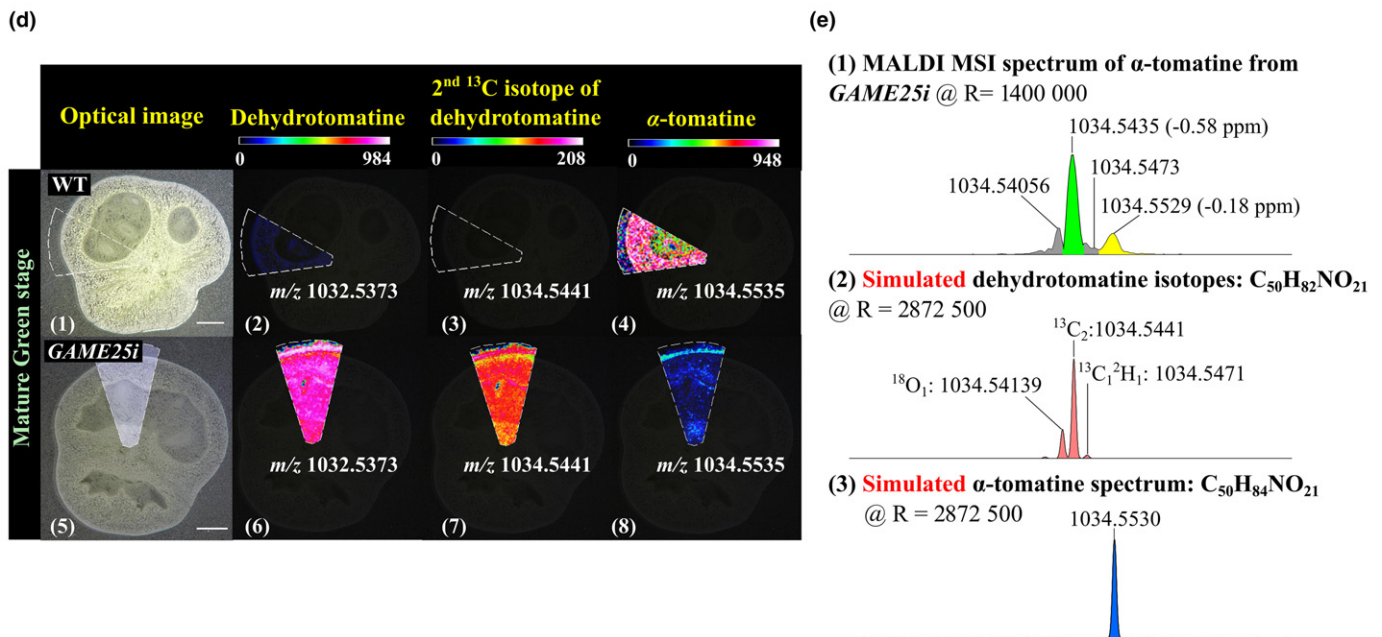


Fig. 2 MALDI imaging of dehydrotomatine and α -tomatine in wild-type (WT) and *GAME25i* mature green tomato fruits. High mass resolution MALDI imaging was performed at mass resolution $R = 115\,000$ (at m/z 400). (a) MALDI images of dehydrotomatine (2, 5) and α -tomatine (3, 6) in wild-type (1) and *GAME25i* fruits (4). (b) Representative MALDI imaging mass spectra of α -tomatine and dehydrotomatine from wild-type and *GAME25i* fruits. (c) Comparison of ion peak m/z 1034.5446 with simulated second ^{13}C isotope peak of dehydrotomatine ($^{12}\text{C}_{48}^{13}\text{C}_2\text{H}_{82}\text{NO}_{21}$, $[\text{M}+\text{H}]^+$, theoretical m/z 1034.5441) and simulated α -tomatine peak ($\text{C}_{50}\text{H}_{84}\text{NO}_{21}$, $[\text{M}+\text{H}]^+$, theoretical m/z 1034.5530). Ultra-high mass resolution MALDI imaging was performed at mass resolution $R = 1400\,000$ (at m/z 400). (d) Comparison of α -tomatine peak (m/z 1034.5529) with simulated second ^{13}C isotope peak of dehydrotomatine ($^{12}\text{C}_{48}^{13}\text{C}_2\text{H}_{82}\text{NO}_{21}$, $[\text{M}+\text{H}]^+$, theoretical m/z 1034.5441) and simulated α -tomatine peak ($\text{C}_{50}\text{H}_{84}\text{NO}_{21}$, $[\text{M}+\text{H}]^+$, theoretical m/z 1034.5530). (e) MALDI images of dehydrotomatine (2, 6), second ^{13}C isotope of dehydrotomatine (3, 7), and α -tomatine (4, 8) in wild-type (1) and *GAME25i* fruits (5). MALDI images were generated with 65 μm spatial resolution, and m/z bin width of $\Delta m/z = \pm 5$ ppm for $R = 115\,000$, and $\Delta m/z = \pm 1$ ppm for $R = 1400\,000$. Scale bar, 2 mm. The blue-red rainbow colour scale indicates the range of root-mean-square normalised intensity. The same metabolite is visualised under identical scale intensity for their semiquantitative comparison. It should be noted that it is not straightforward to compare the relative abundance of different metabolites using MALDI images due to the reason that their ionisation efficiencies may be different.

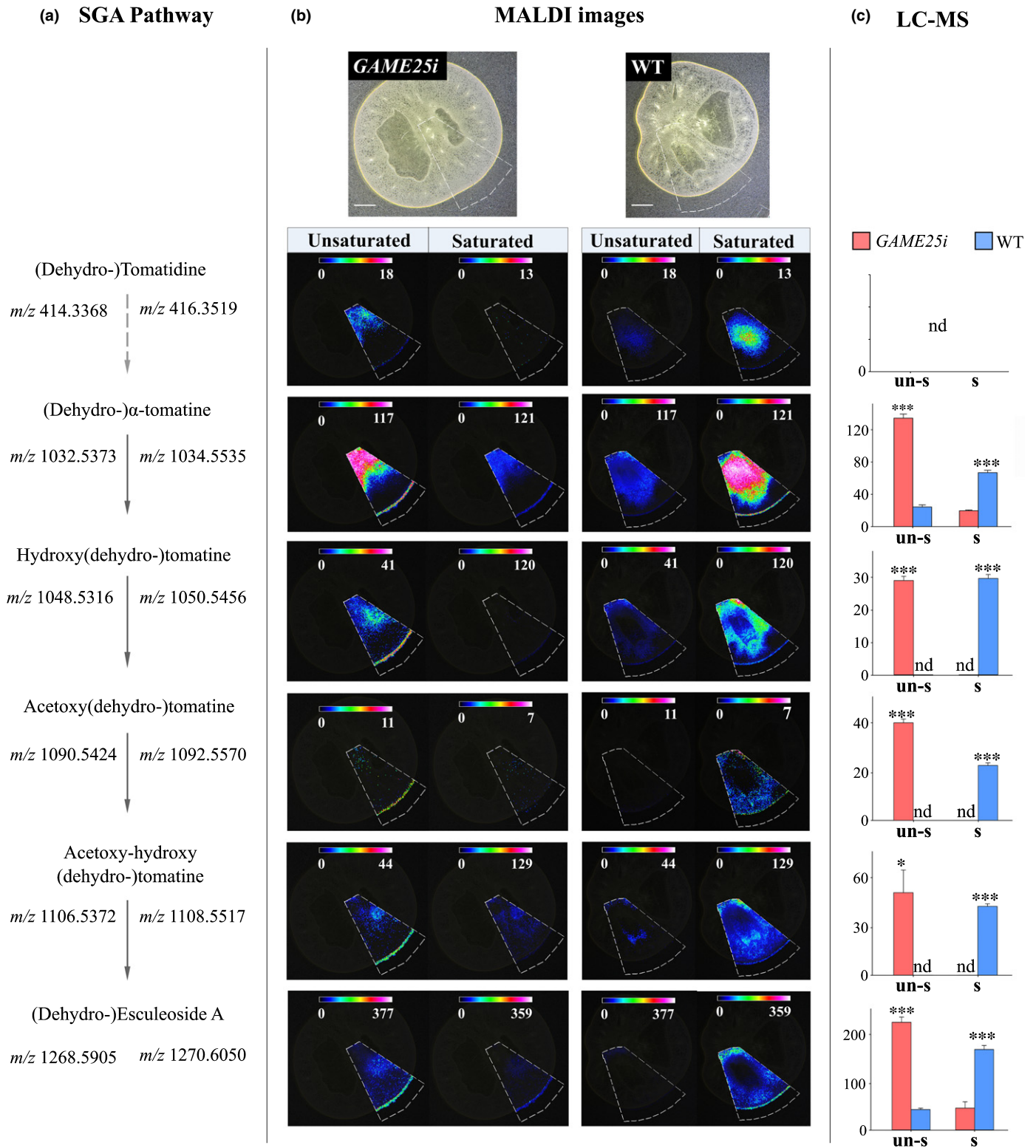


Fig. 3 Visualisation of steroidal glycoalkaloid (SGA) pathway in wild-type (WT) and *GAME25i* mature red ripe tomato fruits using MALDI imaging and LC-MS. (a) Simplified SGA pathway in tomato fruit. (b) MALDI images of SGAs in WT and *GAME25i* tomato fruit. MALDI images were generated with 65 μ m spatial resolution, and m/z bin width of $\Delta m/z = \pm 1$ ppm. Bars, 2 mm. The blue-red rainbow colour scale indicates the root mean square normalised intensity. The same SGA was visualised under identical scale intensity to allow semiquantitative comparison. It should be noted that it is not straightforward to compare the relative abundance of different metabolites using MALDI images as their ionisation efficiencies may be different. (c) Comparison of SGA levels between WT and *GAME25i* using LC-MS. Bar plot represents mean + SD ($n = 3$) of square root transformed peak area (LC-MS). Asterisks denote significant differences (*, $P < 0.05$, **, $P < 0.01$, ***, $P < 0.0001$; Wilcoxon signed-rank test) between WT and *GAME25i* tomato fruit. nd, not detected.

time increased from 2 h to more than 20 h when mass resolution was changed from $R=115\,000$ to $R=1\,400\,000$ at $m/z\,400$.

Combining VIGS with MALDI imaging to uncover gene–metabolite relationship

As a complement to other reverse genetics approaches, VIGS transiently downregulates the expression of candidate genes in intact plant tissues, generating loss-of-function phenotypes within several weeks (Orzaez *et al.*, 2009; Fantini *et al.*, 2013). One technical limitation associated with VIGS is that the penetration of VIGS-silenced phenotype is irregular and shows patchy tissue distribution in most plant species (Orzaez *et al.*, 2009), which complicates the dissection of nonvisual silenced phenotype for subsequent metabolite analysis. This limitation has been alleviated in tomato by fruit-specific overexpression of the *Del* and *Ros1* transcription factors that trigger the accumulation of anthocyanins to form purple-fruited phenotype in tomato plants (E8: *Del/Ros1*), and the modification of the VIGS vector to contain partial *Del* and *Ros1* genes sequences for silencing. Co-silencing of *Del/Ros1* and the gene of interest (GOI) prevents anthocyanin pigments accumulation, leading to red-fruited phenotype in tomato. In this way, anthocyanin pigmentation serves as a visual reporter to guide the dissection of silenced, anthocyanin-free sectors from nonsilenced, anthocyanin-containing sectors (Orzaez *et al.*, 2009; Fantini *et al.*, 2013) (Fig. 4b).

The use of anthocyanin-guided VIGS, however, does not completely circumvent this limitation, as there are no clear boundaries between silenced and nonsilenced sectors. Compared with LC-MS or GC-MS analysis of sample extracts, MSI does not require manual tissue dissection of silenced or nonsilenced regions. Instead, the co-existence of multiple phenotypes in the same sample facilitates the quantitative comparison of different phenotypes, because the intersample variations and batch effects are eliminated. Burkhow and colleagues (Burkhow *et al.*, 2018) spatially characterised the biochemical changes in maize leaves following VIGS-based silencing using multimodal Raman and MALDI imaging. In a similar manner, by combining VIGS, MALDI imaging and LC-MS we studied *GAME31*, a 2-oxoglutarate dependent dioxygenase, catalysing the hydroxylation of α -tomatine to hydroxytomatine in the tomato esculeoside A biosynthetic pathway (Cárdenas *et al.*, 2019) (Fig. 4a). Tomato fruit (E8: *Del/Ros1*) were agroinfiltrated at the mature green stage using a tobacco rattle virus (TRV) vector carrying fragments of the *Del/Ros1* and *GAME31* genes. Following 3–4 wk of infection, fruit showed clear visible red sectors on the background of purple fruit (nonsilenced sectors) (Fig. 4b). To assess whether VIGS by itself has any influence on SGAs metabolism, E8: *Del/Ros1* tomato fruit infected with the TRV plasmid harbouring merely the *Del/Ros1* sequence (without the GOI) were used as a control. PCA of metabolic profiles showed that nonsilenced sectors from control and *GAME31*-VIGS tomato fruits were clustered together, while VIGS-silenced sectors from control and *GAME31*-VIGS tomato fruits were clearly separated (Fig. S4).

We first mapped the distribution of anthocyanins in VIGS-silenced tomato fruit. Due to the positive charge on the C ring,

anthocyanins were readily detected as radical ions in the positive ion mode. Delphinidin ($m/z\,303.0500$, $[M]^+$), petunidin ($m/z\,317.0656$, $[M]^+$) and malvidin ($m/z\,331.0812$, $[M]^+$) were the three major anthocyanidins found in purple sectors of *GAME31*-VIGS and control tomato fruit. In total, 7 and 10 anthocyanins were identified using MALDI imaging and LC-MS, respectively, which were the combination of the three anthocyanidins and their glycosyl and acyl moieties (Tables S3, S4). Anthocyanins are prone to in-source fragmentation during MALDI analysis and the fragmentation efficiency of each individual anthocyanins can vary significantly among samples (Wang *et al.*, 2000), therefore semiquantitative assessment of each anthocyanin is challenging. Nevertheless, the distribution patterns of each anthocyanidin (the anthocyanin aglycone) were found to be nearly identical to their corresponding anthocyanins. Consequently, the distribution of the three anthocyanidins was used to represent the spatial accumulation of anthocyanin. As shown in Fig. 5a, distribution of the three anthocyanidins was all well correlated with the localisation of the purple colour, and their ion intensities increased with the level of purple pigmentation. Semiquantitative comparisons using MALDI and LC-MS confirmed that anthocyanidins were significantly higher in nonsilenced sectors ($P < 0.001$) (Fig. 5b, d). Apart from their introduction as visual reporters to guide tissue dissection, anthocyanins are also ideal quality controls for the assessment of MALDI imaging performance as they are coloured compounds and their distribution can be easily resolved by the naked eye.

Next, we compared the SGA profile between silenced and nonsilenced sectors in control tomato fruit to check whether VIGS by itself affects SGA metabolism. As mentioned previously, α -tomatine is the predominant SGA in green tomato fruit and is converted to esculeoside A during maturation. The content of α -tomatine in green fruit could reach up to 500 mg kg^{-1} of fresh fruit weight, which is then reduced to $c. 5\text{ mg kg}^{-1}$ of fresh fruit weight in mature red ripe fruit (Mintz-Oron *et al.*, 2008; Friedman, 2013). Both α -tomatine and esculeoside A were detected in mature control fruit using MALDI imaging. Esculeoside A was localised homogeneously between silenced and nonsilenced sectors, while only trace amounts of α -tomatine were detected (Fig. 5a). Nevertheless, MALDI imaging and LC-MS results showed that there were no statistically significant differences in levels of the two major SGA contents between silenced and nonsilenced sectors in mature fruit, suggesting that VIGS by itself does not affect SGAs metabolism.

Compared with control fruit, high levels of α -tomatine were detected in *GAME31*-VIGS mature fruit (Fig. 5c,d). The MALDI image showed that α -tomatine was mostly localised in *GAME31*-VIGS-silenced sectors and its content was negatively correlated with the abundance of anthocyanins (Fig. 5c). Relative quantification of MALDI imaging and LC-MS data showed that α -tomatine content was significantly higher ($P < 0.01$) in silenced sectors compared with nonsilenced sectors (Fig. 5d). Apart from α -tomatine, three additional upstream SGAs, namely dehydrotomatidine, tomatidine, and dehydrotomatine (Fig. S5, and see SGA pathway in Fig. 1), were also exclusively localised in silenced sectors of *GAME31*-VIGS tomato fruit. However, the contents

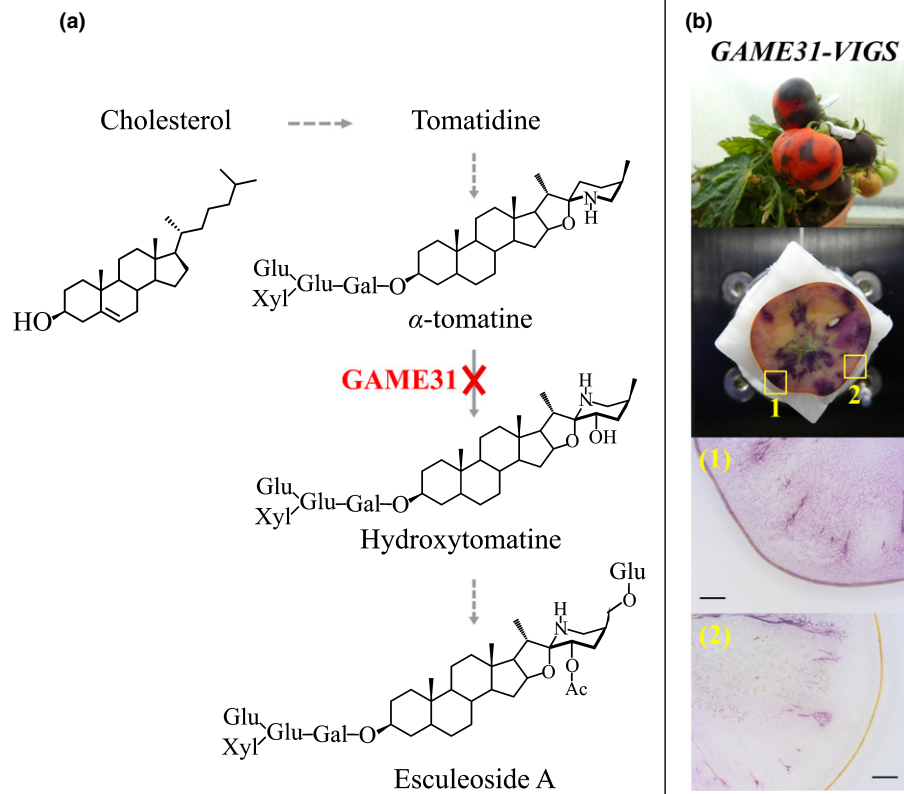


Fig. 4 Anthocyanin-mediated visualisation of *GAME31* gene virus induced gene silencing (VIGS) in tomato fruits. (a) Wild-type (WT) tomato fruits were subject to VIGS assay at mature green stage using a TRV vector carrying fragments of the *Del* and *Ros1* visual reporter genes and a *GAME31* fragment. As a consequence, the conversion of α -tomatine to its downstream hydroxy- and acetoxy-derivatives were blocked. (b) The nonuniform accumulation of anthocyanins distinguishes the nonsilenced (1: anthocyanin-rich) and silenced (2: anthocyanin-free) sectors in the same tomato fruit. Bars, 100 μ m.

of downstream SGAs, for example esculeoside A, were not found to be significantly reduced in silenced sectors of mature red ripe *GAME31*-VIGS fruit (Fig. 5d). This might be because the reduction in *GAME31* expression by VIGS silencing is not strong enough and/or activities of *GAME31*-like genes compensate the production of downstream SGAs.

As discussed previously, functions of many genes remain elusive, because either their corresponding metabolites are unknown or the gene–metabolite relationship is unclear. As demonstrated in this example, the combination of VIGS with MALDI imaging provides a direct way to investigate the exact gene–metabolite relationship, as the distribution patterns of the corresponding metabolites were found to be highly correlated to the gene silencing pattern (i.e. anthocyanin-free sectors). In addition, this strategy can also be applied in untargeted MSI analysis for discovering novel gene-related metabolites by screening for metabolites with highly positive or negative correlation to a specific gene expression pattern (Horn & Chapman, 2014b) (nontargeted approach with MSI, to be described later).

Coupling agroinfiltration with MALDI imaging for rapid gene function analysis

In addition to VIGS, transient expression of exogenous genes in plant tissues such as agroinfiltration (*Agrobacterium*-mediated

gene expression) is another powerful tool to assess gene function (Wroblewski *et al.*, 2005). Betalains are tyrosine-derived pigments widely used as natural colourants, strong antioxidants and health-promoting compounds (Gandía-Herrero & García-Carmona, 2013; Polturak & Aharoni, 2018). According to their chemical structure, betalains can be classified into red-violet betacyanins and yellow betaxanthins. Betacyanins are iminium adducts of betalamic acid and cyclo-dihydroxyphenylalanine (cyclo-DOPA), whereas betaxanthins are biosynthesised by condensation of α -amino acids or amines with betalamic acid (Polturak *et al.*, 2016) (Fig. 6). Despite their great potential in food, industrial and pharmaceutical applications, betalains have not been as well studied compared with other plant pigments, i.e. anthocyanins and carotenoids (Tanaka *et al.*, 2008). MALDI imaging has been used to compare the accumulation of lipid droplets and spatial distribution of different triacylglycerol (TAG) molecular species between wild-type and transgenic *N. benthamiana* leaf tissues (Vanhercke *et al.*, 2014). In this example, we employed agroinfiltration to produce betalains in *N. benthamiana* leaves and examined the use of MALDI-imaging to detect metabolic changes in infiltrated leaves. Co-infiltration of the red beet *BvDODA1* and *CYP76AD1* genes and the *Mirabilis jalapa* *cDOPA5GT* gene leads to the production of betacyanins (pX11 plasmid; Fig. 6), while expression of *CYP76AD6* and *BvDODA1* results in the accumulation of betaxanthins (pX13 plasmid;

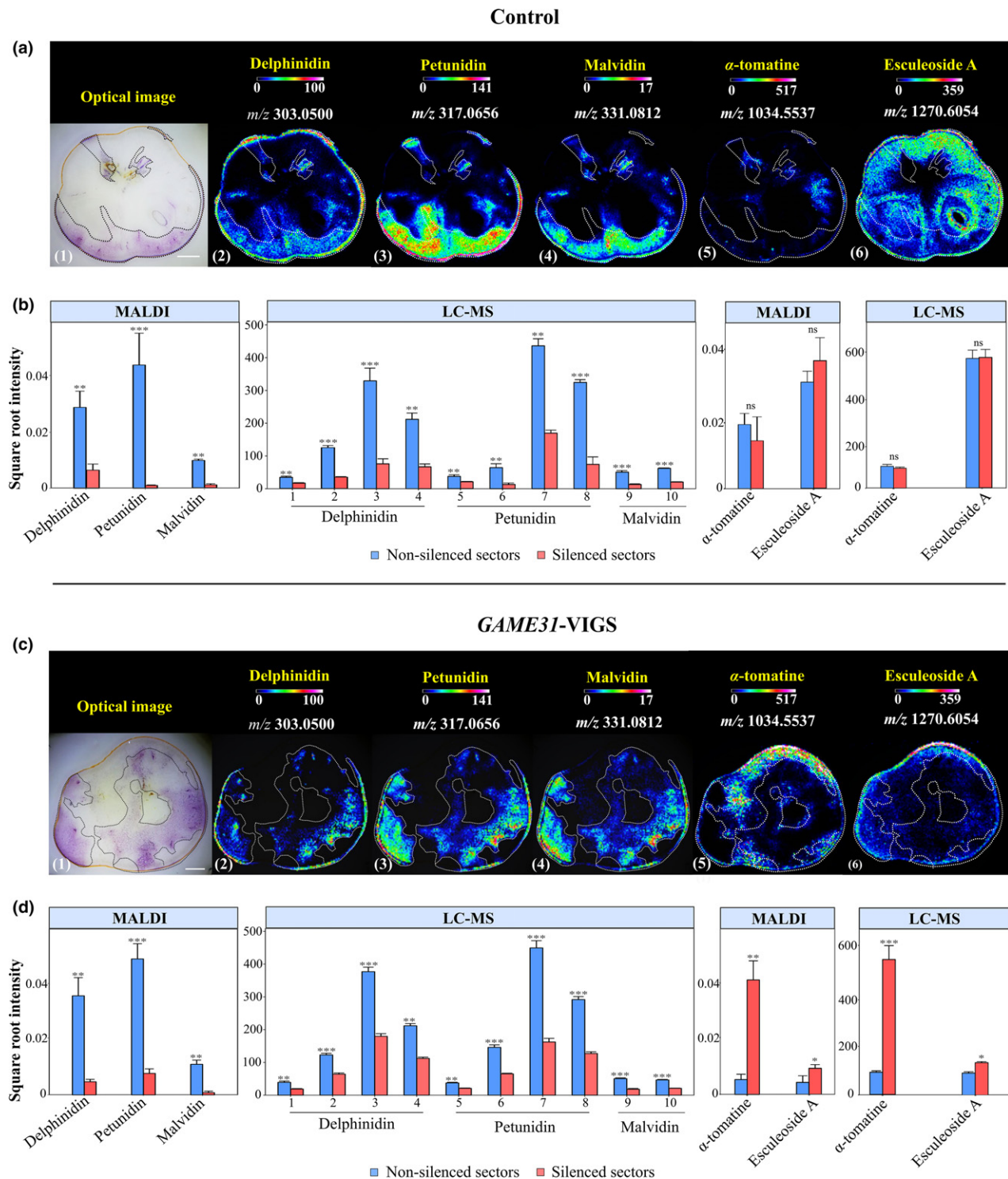


Fig. 5 Localisation and semiquantitative comparison of anthocyanins and major steroidal glycoalkaloids (SGAs) in control and *GAME31-VIGS* mature red ripe tomato fruits using MALDI imaging and LC-MS. (a, c) Optical images of control and *GAME31-VIGS* tomato fruits (1). MALDI images of delphinidin (2), petunidin (3), malvidin (4), α -tomatine (5) and esculeoside A (6) in control and *GAME31-VIGS* tomato fruits. MALDI images were generated with 150 μm spatial resolution, and m/z bin width of $\Delta m/z = \pm 5$ ppm. Bars, 5 mm. The blue-red rainbow colour scale indicates the range of root-mean-square normalised intensity. The same metabolite was visualised under identical intensity scale in order to allow semiquantitative comparison. It should be noted that it is not straightforward to compare the relative abundance of different metabolites using MALDI images as their ionisation efficiencies may be different. (b, d) Comparison of delphinidin, petunidin, malvidin, α -tomatine and esculeoside A levels between nonsilenced and silenced sectors in control and *GAME31-VIGS* tomato fruits using MALDI imaging and LC-MS. Bar plot represents the mean + SD ($n = 3$) of square root transformed ion intensity (MALDI) or peak area (LC-MS). Asterisks denote significant differences (ns: not significant; *, $P < 0.05$; **, $P < 0.01$; ***, $P < 0.0001$; Wilcoxon signed-rank test) between nonsilenced and silenced sectors in control and *GAME31-VIGS* tomato fruits.

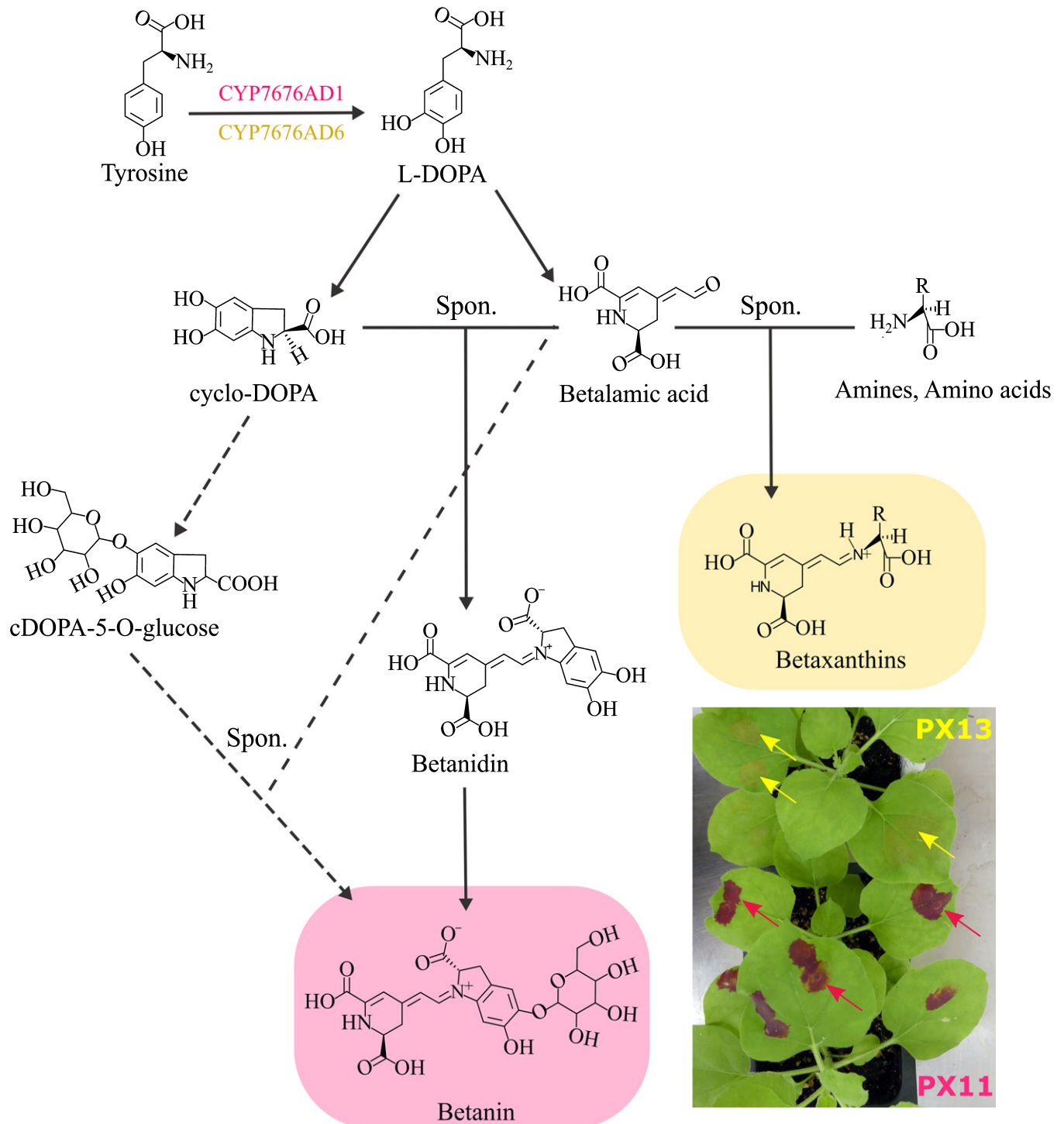


Fig. 6 Agroinfiltration-based transient expression of cytochrome P450s CYP76AD1 and CYP76AD6 in *Nicotiana benthamiana* leaves enables betalain biosynthesis. L-DOPA is produced from tyrosine by the cytochrome P450 enzymes CYP76AD1 or CYP76AD6. Subsequently, L-DOPA is converted to cyclo-DOPA (cDOPA) or betalamic acid. Betalamic acid then spontaneously conjugates with amino acids and amine groups to generate yellow betaxanthins, or cyclises with cDOPA to form betanidin, which is the aglycone precursor for red-violet betacyanins. Dashed lines designate reactions of an alternative pathway for the formation of betanin, where cyclo-DOPA is first glycosylated and then condenses with betalamic acid. Expression of the pX11 vector mainly results in production of betacyanins, while pX13 expression leads to formation of betaxanthins in *N. benthamiana* leaves. Spon., spontaneous condensation reactions.

Fig. 6). Infiltration of an empty vector (3α1) was used as a control to exclude possible mass signals that are produced upon infiltration but not directly related to betalain biosynthesis.

Ideally, we would like to map the distribution of betalains in intact *N. benthamiana* leaves without cryo-sectioning. However, the presence of leaf cuticle hinders the direct metabolite analysis

by MALDI imaging, because the laser cannot easily penetrate the leaf cuticle (Dong *et al.*, 2016b). Physical (e.g. pressing the leaf with a metal plate) or chemical (e.g. chemical wash with chloroform for 10 s) removal of the leaf cuticle indeed permitted direct detection of betalains, but the ion signals were too low and usually unstable, resulting in poor quality images (Fig. S6). Nevertheless, betalains were readily detected as protonated ions ($[M+H]^+$) in cryo-sectioned leaves of infiltrated *N. benthamiana* using MALDI imaging. Four betacyanins, including betanin (m/z 551.1505, $C_{24}H_{26}N_2O_{13}$), betanidin (m/z 389.0978, $C_{18}H_{16}N_2O_8$), and two unknown betacyanins (unknown betacyanin I: m/z 670.1874, $C_{31}H_{31}N_3O_{14}$ and unknown betacyanin II: m/z 655.1773, $C_{31}H_{30}N_2O_{14}$) were exclusively identified in pX11-infiltrated leaf sections (Table S5). Localisation of betacyanins was highly correlated with the spatial distribution of the red-violet coloration (Fig. 7a). Similarly, three betaxanthins were detected in pX13-infiltrated leaf areas including vulgaxanthin (m/z 340.1138, $C_{14}H_{17}N_3O_7$), dopaxanthin-hexoside (m/z 391.1132, $C_{18}H_{18}N_2O_8$) and one unknown betaxanthin (m/z 342.1147, $C_{18}H_{19}N_3O_4$) (Table S5). MALDI imaging showed that betaxanthins accumulated exclusively in the infiltrated leaf areas (Fig. 7a). In addition, betalamic acid (m/z 212.0553, $C_9H_9NO_5$), an intermediate in the betaxanthin biosynthetic pathway, was also found localised merely in infiltrated leaf areas of pX13 *N. benthamiana*. As in the case of anthocyanins and VIGS in tomato fruit, chlorophyll a was also used here for initial evaluation of MALDI imaging performance because its distribution could be visually resolved and was not affected by agroinfiltration. Indeed, MALDI images showed that chlorophyll a ($[M+H]^+$, m/z 893.549, $C_{55}H_{73}MgN_4O_5$) was homogeneously distributed in the pX11- and pX13-expressing leaf sections (Fig. 7a), indicating that the performance of the entire MALDI imaging system was optimal.

LC-MS extract analysis of infiltrated *N. benthamiana* leaves confirmed the results from MALDI imaging, except that an additional betanin isomer (iso-betanin, RT = 9.38 min, m/z 551.1509, $C_{24}H_{26}N_2O_{13}$) and one extra vulgaxanthin isomer (iso-vulgaxanthin, RT = 2.74 min, m/z 340.1145, $C_{14}H_{17}N_3O_7$) were detected in pX11 and pX13 leaves, respectively (Table S6). The inability of distinguishing most isomers by MSI has been well documented (elaborated further below). Nevertheless, MALDI imaging and LC-MS results are in good agreement that all detected betacyanins and betaxanthins are statistically significantly higher ($P < 0.01$) in infiltrated leaf areas of pX11 and pX13 *N. benthamiana* (Fig. 7b). Plant pigments include various

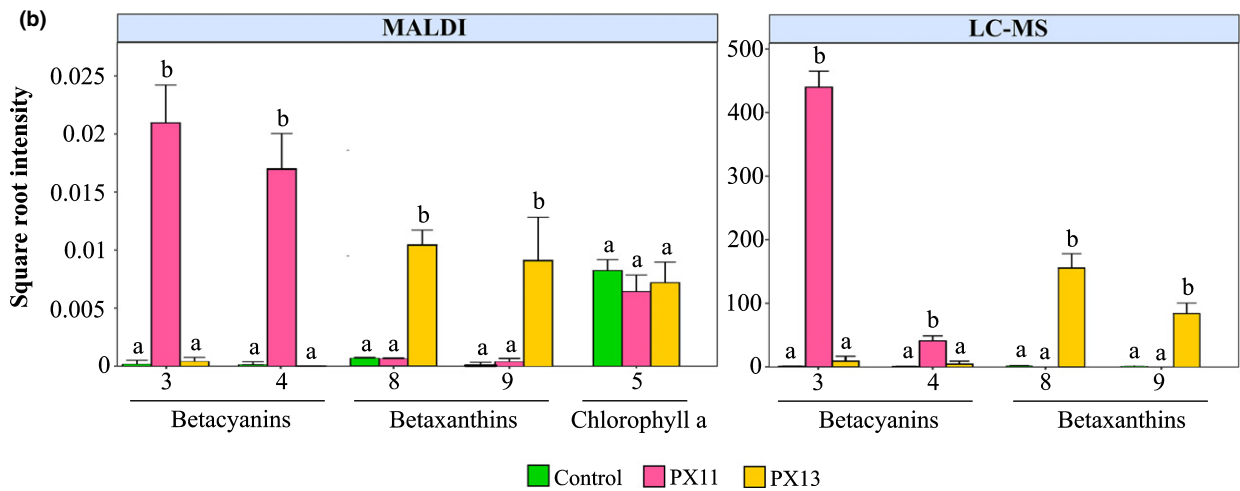
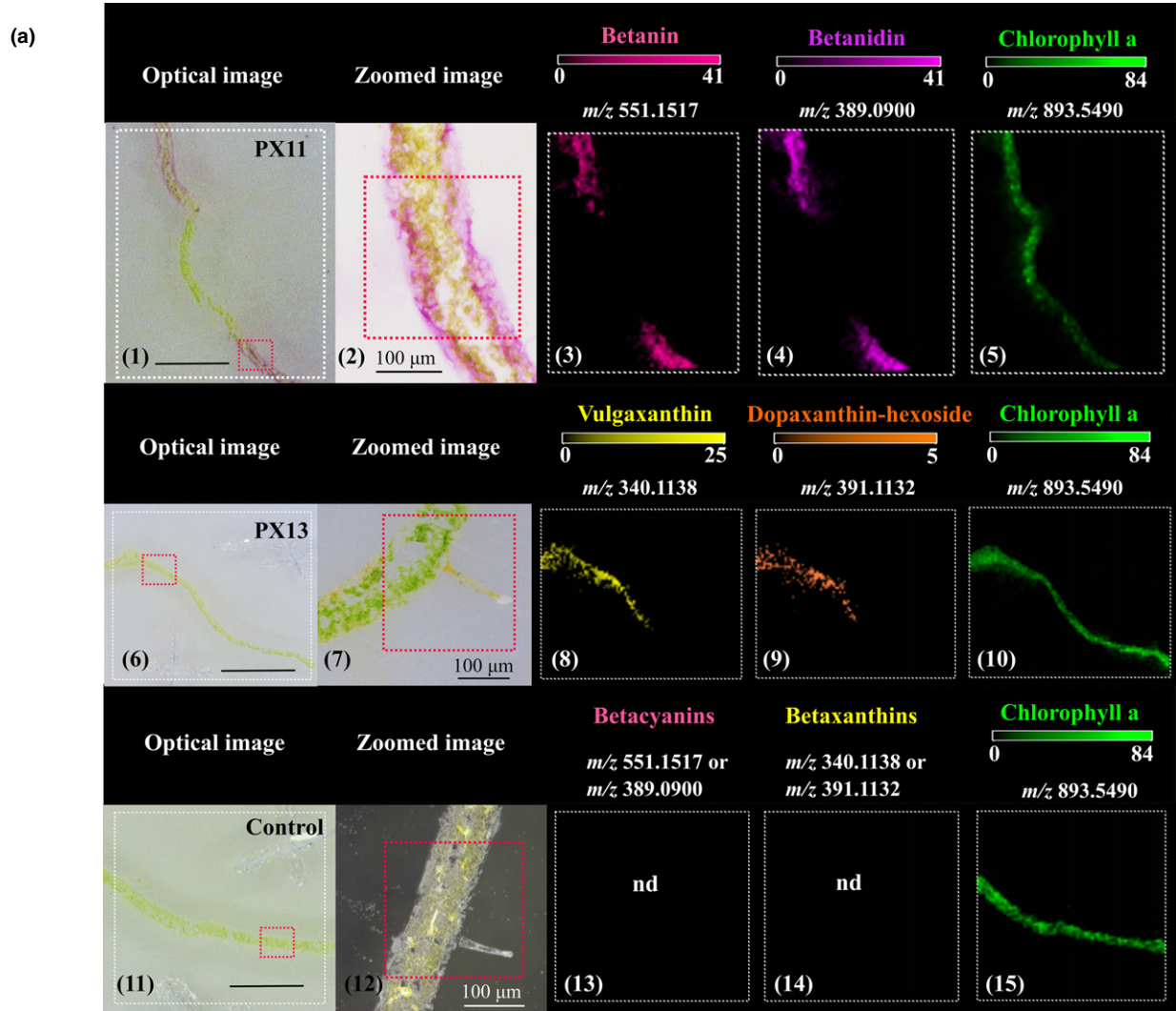
compounds of a wide range of polarities from nonpolar carotenoids and chlorophylls to polar anthocyanins and betalains. This makes their simultaneous detection using a single LC-MS workflow impossible. For instance, the dedicated LC-MS method used here for betalain detection is unable to detect any chlorophylls from *N. benthamiana* leaves (Fig. 7b). By contrast, our previous results have shown that all the four major classes of plant pigments, that is anthocyanins, carotenoids, betalains and chlorophylls, can be detected simultaneously in a single MALDI imaging analysis (Polturak *et al.*, 2017). In addition, the spatial information obtained from MALDI imaging can be also used to assist metabolite identification. For instance, in LC-MS three unknown peaks: (1) unknown betacyanin I: RT = 13.04 min, m/z 670.1873, $C_{31}H_{31}N_3O_{14}$; (2) unknown betacyanin II: RT = 16.12, m/z 655.1769, $C_{31}H_{30}N_2O_{14}$; and (3) an unknown betaxanthin: RT = 6.86 min, m/z 342.1454, $C_{18}H_{19}N_3O_{14}$, were assigned as betalains based on their typical betalain UV-vis absorptions (λ_{max} c. 535 nm for betacyanins, and λ_{max} c. 480 nm for betaxanthins) and characteristic MS/MS fragments (Table S5). The high correlation between the spatial distribution of the three unknown ions and the area of pigmentation corroborates the identity of these ions as betalain related.

As agroinfiltration enables the introduction of multiple vectors into different areas of a single leaf (Vaghchhipawala *et al.*, 2011), we anticipate that the coupling of MSI with agroinfiltration can be applied in a microarray-like approach for conducting multiple assays on the same sample. Compared with LC-MS, coupling MSI with agroinfiltration provides a rapid and efficient approach for primary characterisation of candidate gene function, gene product detection and localisation.

High mass accuracy MSI phenotyping of wheat epicuticular waxes

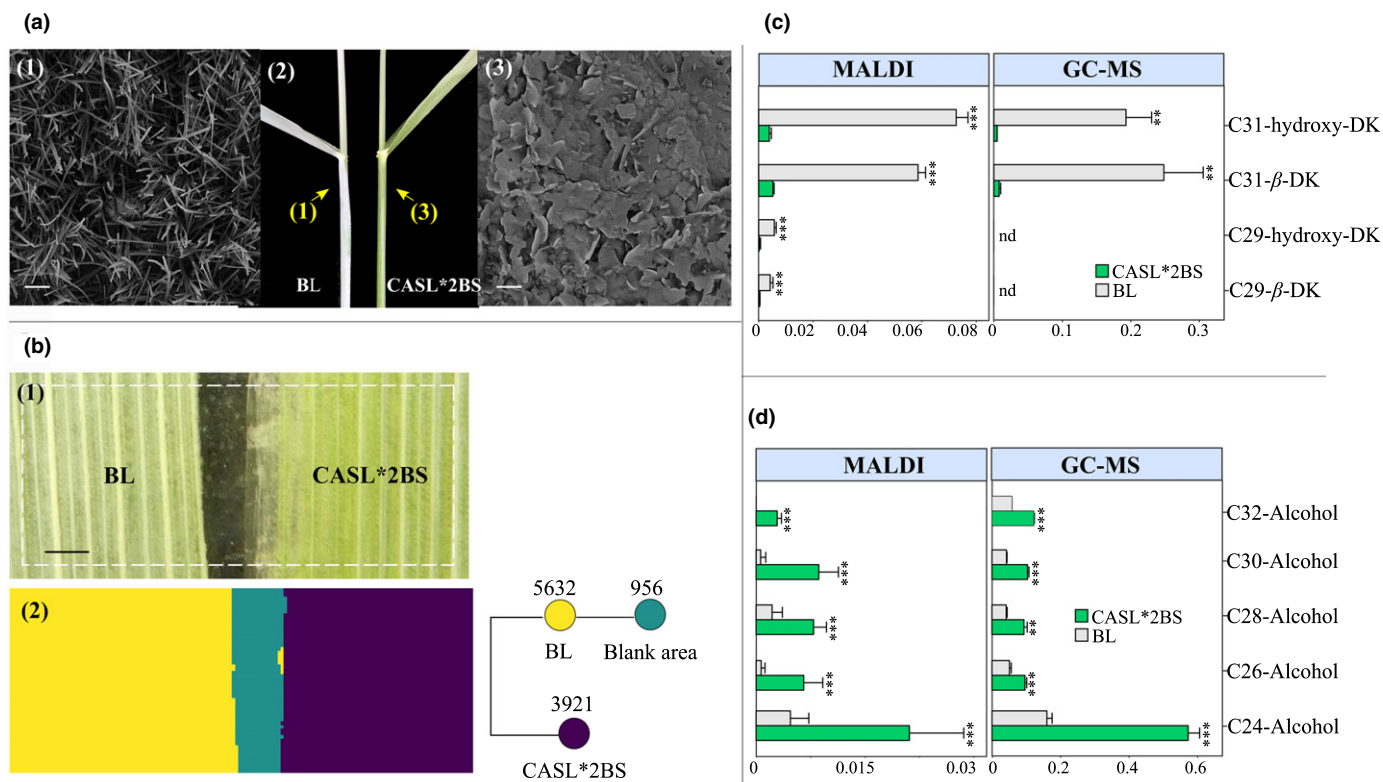
Apart from artificially generated mutations, naturally occurring genetic variants are available for many plant species (Koorneef *et al.*, 2004; Alonso-Blanco *et al.*, 2009). Hence, natural variants provide another important source to identify multiple allelic differences that contribute to a single trait or phenotypic variation. Epicuticular waxes (EW) are specialised compounds deposited on the outer surface of plant cuticles that function as a protective layer against various environmental cues (Eigenbrode & Jetter, 2002; Huang *et al.*, 2017). In wheat, β -diketones are major EW components providing blue-grey coloration (glaucous) to stems, leaves and flower heads (Huang *et al.*, 2017). The opposing

Fig. 7 Localisation and semiquantitative comparison of betalains and chlorophyll a in agroinfiltrated *Nicotiana benthamiana* leaves using MALDI imaging and LC-MS. (a) MALDI imaging of PX11-, PX13-expressing and control *N. benthamiana* leaves. (1), (6) and (11) are optical images of PX11-, PX13-expressing and control *N. benthamiana* leaf sections; (2), (7) and (12) are their zoomed images. The MALDI images showed that betacyanins (3, 4) and betaxanthins (8, 9) were exclusively synthesised in PX11 and PX13 agroinfiltrated areas of *N. benthamiana* leaves, respectively. Chlorophyll a was used as a quality control, and it was found homogeneously distributed in the leaf sections. MALDI images were generated with 60 μ m spatial resolution, and m/z bin width of $\Delta m/z = \pm 5$ ppm. Bars, 1 mm. The colour scale indicates the range of root-mean-square normalised intensity. The same metabolite was visualised under identical intensity scale in order to allow semiquantitative comparison. It should be noted that it is not straightforward to compare the relative abundance of different metabolites using MALDI images as their ionisation efficiencies may be different. (b) Semiquantitative comparison of betacyanins (3–4), betaxanthins (8–9) and chlorophyll a (5) from agroinfiltrated areas of PX11-, PX13-expressing and control *N. benthamiana* leaves using MALDI imaging and LC-MS. Bar plot represents mean + SD ($n = 3$) of square root transformed ion intensity (MALDI) or peak area (LC-MS). Different letters denote significant differences ($P < 0.01$, Kruskal–Wallis test) among infiltrated areas of PX11, PX13 expressing and control *N. benthamiana* leaves. nd: not detected.



phenotype is known as nonglaucous or glossy, which is used to describe plants that show a bright-green colour (Hen-Avivi *et al.*, 2016). Both glaucous and glossy phenotypes are present among wild wheat species. Here we compared the composition,

abundance and distribution of the EW between the glaucous Bethlehem BL (BL) and the glossy CASL*2BS wheat lines (Rong *et al.*, 2000) (Fig. 8a) using MALDI imaging and GC-MS. EWs have been studied extensively using a brief chloroform extraction



followed by GC-MS analysis. However, as chloroform can rapidly penetrate the deeper layers of the cuticle and indiscriminately extract both epi- and intracuticular waxes, the resulting extracts typically represent the total wax composition rather than the composition of the EW alone (Jetter & Schäffer, 2001; Buschhaus *et al.*, 2007). By contrast, MALDI imaging provides a selective approach to determine the chemical composition of the EW, as its laser ablation depth is *c.* 50–200 nm (Dreisewerd, 2003), which is in accordance with the typical thickness of this layer (up to 240 nm in wheat; Fernández *et al.*, 2014).

Cryo-scanning electron microscopy (cryo-SEM) indicated that the flag leaf sheaths of the BL cultivar are covered with tube-shaped EW crystals that are typical for β -diketones deposition. The flag leaf sheaths of CASL*2BS, conversely, largely accumulate platelet-shaped crystals associated with the abundance of alcohol-rich wax (Bianchi & Figini, 1986; Hen-Avivi *et al.*, 2016) (Fig. 8a). To minimise the batch effects and any variations that could arise during sample preparation, we dissected the flag leaf sheaths from both BL and CASL*2BS cultivars, and attached them onto the same glass slide. They were then analysed by MALDI imaging as ‘one sample with two phenotypes’ (Fig. 8b) in a similar manner as described for VIGS in tomato and

agroinfiltrated *N. benthamiana* leaves. The acquired MALDI imaging data were first examined using bisecting k-means clustering to obtain image segmentation of the two wheat lines according to their chemical composition. This procedure clustered all MS spectra into different groups based on their similarity, and each group was assigned a specific pseudocolour (Fig. 8b). The resulting segmentation map well represents the morphological regions of the sample with three clusters: the yellow cluster denotes BL flag leaf, the purple denotes CASL*2BS flag leaf, and the green denotes the blank region between the two tissues (Fig. 8b).

In addition to highlighting the distinct anatomical regions, the segmentation map can also be used to identify mass peaks associated with these regions. In total, 106 mass peaks (after ^{13}C -deisotoping) were found to be highly co-localised with either BL or CASL*2BS flag leaf sheaths with Pearson correlation coefficient higher than 0.85 and a P -value ≤ 0.05 . In total, 95 of them were tentatively identified based on accurate mass and isotope pattern from MALDI imaging, GC-MS results of the tissue extracts, and previous reports (Racovita & Jetter 2016) (Tables S7, S8). Among them, 48 mass peaks corresponding to 21 metabolites were found to be co-localised in the BL flag leaf sheath. They

were distributed homogeneously over the leaf sheath, with C31 hydroxy- β -diketone and C31 β -diketone being the predominant metabolites. The result was in good agreement with GC-MS data and previous reports, showing that these two compounds make up 79% of the total wax amount, and are responsible for the glaucous appearance of BL wheat cultivar (Zhang *et al.*, 2013; Hen-Avivi *et al.*, 2016; Huang *et al.*, 2017) (Fig. 8c). In addition, trace amounts of C29 hydroxy- β -diketone and C29 β -diketone were only detected by MALDI imaging, demonstrating its complementarity to GC-MS in metabolite detection. Conversely, 48 mass peaks, corresponding to 25 metabolites, were found co-localised with CASL*2BS flag leaf sheath. Among them, C24, C26, C28, C30 and C32 primary alcohols were the prevalent wax species, which is in agreement with GC-MS data and the previous reports showing that the absence of β -diketones is compensated by an increase of primary alcohols (Zhang *et al.*, 2013; Hen-Avivi *et al.*, 2016). Previous results have suggested that three candidate genes, namely, *Diketone Metabolism-PKS* (DMP), *Diketone Metabolism-Hydrolase* (DMH) and *Diketone Metabolism-CYP450* (DMC), encode enzymes responsible for β -diketone biosynthesis, and that they are significantly expressed in glaucous BL but repressed in glossy CASL*2BS (Hen-Avivi *et al.*, 2016). Here the correlation of the three gene expression patterns with β -diketone accumulation revealed by MALDI imaging further supports their functions in wheat β -diketone production.

Unlike the examples described in previous sections in which the spatial distribution of targeted metabolites was mapped and compared between mutants and controls, here an untargeted approach was applied using spatial segmentation to find all relevant biomarkers that distinguish the glaucousness and glossiness phenotypes in wheat flag leaf sheaths. It is important to note that the use of high mass resolution, high mass accuracy and lock mass functionality allows direct determination of elemental composition of most biomarkers with $m/z < 550$ Da within 1 ppm mass accuracy in MALDI imaging (Table S8). As elemental composition is the foundation of any further identification, the capability of direct assignment of elemental composition greatly facilitates the process of biomarker identification in MS imaging.

Discussion

Despite its untargeted nature, MSI is still mostly used for targeted analysis, which limits its power in discovering novel gene-associated metabolites. The lack of such 'discovery' type analysis in MSI is mainly due to: (1) difficulty in high confidence metabolite identification; and (2) the number of detected metabolites is relatively low (Dong *et al.*, 2016a). Unlike LC- or GC-MS, MSI analyses molecules directly on a sample tissue surface without any prior extraction or chromatographic separation. Therefore, molecules are annotated only based on their m/z values, isotopic distribution and tandem MS fragmentation patterns. The use of high mass resolution and high mass accuracy mass spectrometers such as Fourier-transform ion cyclotron resonance (FT-ICR) MS indeed allows the direct determination of elemental composition of small molecules up to 500 Da. Yet, it does not provide unambiguous identification of the compound.

In addition, the lack of chromatographic separation makes MSI prone to ion suppression effects especially in complex biological samples, which deters its capability to detect less abundant molecular species (Dong *et al.*, 2016a). Another major limitation associated with MSI is that it hardly distinguishes isomeric compounds, and this can lead to inaccurate assessment of their spatial distribution. For instance, with LC-MS we have identified two betanin isomers (RT at 8.53 and 9.38 min, $C_{24}H_{26}N_2O_{13}$, $[M+H]^+$) and two vulgaxanthin isomers (RT at 2.08 and 2.74 min, $C_{14}H_{17}N_3O_7$, $[M+H]^+$) from PX11- and PX13-expressing *N. benthamiana* leaves, respectively (Table S6). However, it is practically difficult to study the distribution of each isomer by MALDI imaging, even when tandem MSI is applied as there are no distinctive fragments for each isomer (Table S6). Nevertheless, these isomers are expected to have similar distribution patterns, because their distribution is highly correlated to the pigment localisation. However, it is not always the case that isomeric metabolites show the same distribution pattern. As discussed above due to the positive charge on the C ring of delphinidin, it was readily detected as a radical ion (m/z 303.0499, $C_{15}H_{11}O_7$, $[M]^+$) in the positive ion mode. As a result of in-source fragmentation during MALDI imaging, quercetin, one of the major flavonoid aglycones in tomato, was detected as a protonated ion (m/z 303.0499, $C_{15}H_{11}O_7$, $[M+H]^+$), which possesses the same accurate m/z value as the delphinidin radical ion. In this case, MALDI imaging was unable to differentiate the two ions as well as their spatial localisation. Therefore, the MALDI image of delphinidin shown in Fig. 5 was in fact an overlaid MALDI image of delphinidin and quercetin. However, as nearly no anthocyanins were present in the silenced sectors of control and *GAME31-VIGS* tomato fruit, the ion intensity of m/z 303.0499 in the silenced sectors most likely corresponded to the quercetin ion. It can be seen clearly in Fig. 5a that the ion intensity of m/z 303.0499 was much lower in the silenced sectors compared with that from nonsilenced sectors, suggesting that the ion intensity of delphinidin was significantly higher than that of quercetin. Consequently, delphinidin largely determined the distribution pattern of m/z 303.0499. In addition, the high correlation between the pattern of pigmentation and delphinidin distribution in both control and *GAME31-VIGS* silenced tomato fruit (Fig. 5a,c) also suggested that delphinidin is the dominant ion in the overlaid MALDI image of m/z 303.0499. To further corroborate our conclusion, we used wild-type tomato fruits to study the spatial accumulation of quercetin, as they do not contain any delphinidin. The result showed that quercetin is only present in the tomato fruit epidermis (Fig. S7). By contrast, in control and *GAME31-VIGS* silenced fruit, m/z 303.0499 was detected in the entire fruit section including pericarp and placenta (Fig. 5a,c), indicating that the delphinidin ion was the major contributor to the MALDI image of m/z 303.0499 in nonsilenced sectors of control and *GAME31-VIGS* silenced tomato fruit.

Reverse genetics, the creation of a phenotype by disrupting or modifying a specific gene or gene product, has rapidly become the method of choice for understanding the *in vivo* function of genes (Schwachtje *et al.*, 2008). Once gene expression has been

altered, expression products such as metabolites are quantified and the resultant changes are assessed to infer the gene function (Sumner *et al.*, 2003). MSI could potentially yield a better understanding of gene functions with respect to tissue- or cell-specific genes, as it is able to provide high spatial and temporal resolution images of localised metabolites. In particular, the use of ultra-high mass resolution and high mass accuracy MSI significantly improves metabolite detection, and eliminates interferences from isobaric ions, thus allowing discovery of novel gene-associated metabolites and more accurate gene–metabolite relationship. Currently, there are only few tools available to characterise the spatial localisation of gene expression products at tissue or cellular level (Burkhow *et al.*, 2018). The coupling of MSI with different reverse genetics approaches has provided an rapid and cost-effective way to study gene–metabolite relationship and discover novel gene-associated metabolites. While it is laborious and time-consuming to dissect different phenotypic sectors from samples generated by VIGS or agroinfiltration for LC- or GC-MS analysis, MSI is a perfect tool for such sample types as it does not require any manual tissue dissection and separation, and it is free from batch effects. In cases when gene products are ‘colourless’ and no visible phenotypes are observed, it is advisable to select multiple and large sample areas for imaging analysis in order to capture heterogeneous biochemical responses (Burkhow *et al.*, 2018).

Even though there is still progress to be made in the areas of sample preparation, matrix development, spatial resolution, instrumental sensitivity and speed, to accommodate high throughput analysis and widespread use of MALDI and other MSI technologies (Sturtevant *et al.*, 2016; Qin *et al.*, 2018), MSI is being greatly adopted in plant science to map the distribution of a broad range of chemical compounds. Our examples demonstrate that a wealth of spatial information can be obtained from MSI. If this approach is combined with classical LC-MS or GC-MS and applied on a larger scale, it could be used as an effective spatial metabolomics tool to discover associations of overall metabolic changes with a particular organ, tissue or cell. Thus, in the next decade, MSI will most likely become a routine and essential tool to study gene function.

Acknowledgements


We thank the Tom and Sondra Rykoff Family Foundation Research and the Israeli Centers of Research Excellence (i-CORE) Programme on Plant Adaptation to Changing Environment for supporting the A.A. laboratory activity. A.A. is the incumbent of the Peter J. Cohn Professorial Chair. This work was supported by the Israel Ministry of Science and Technology [grant number 3-14297].

Author contributions

YD designed the study, performed the experiments and wrote the article. PS generated *GAME25i* and *GAME31-VIGS* tomato lines. HC assisted with GC-MS operation. GP generated PX11 and PX13 expressing *N. benthamiana*. LF assisted with MALDI imaging analysis. SHA assisted with GC-MS data analysis. IR

assisted with LC-MS operation. AA designed the study and wrote the article.

ORCID

Asaph Aharoni  <https://orcid.org/0000-0002-6077-1590>
Yonghui Dong  <https://orcid.org/0000-0002-0534-3868>
Liron Feldberg  <https://orcid.org/0000-0003-3612-1421>
Guy Polturak  <https://orcid.org/0000-0001-6317-7266>
Prashant Sonawane  <https://orcid.org/0000-0002-3631-1703>

References

- Alonso-Blanco C, Aarts MGM, Bentsink L, Keurentjes JJB, Reymond M, Vreugdenhil D, Koornneef M. 2009. What has natural variation taught us about plant development, physiology, and adaptation? *Plant Cell* **21**: 1877–1896.
- Bhandari DR, Wang Q, Friedt W, Spengler B, Gottwald S, Römpf A. 2015. High resolution mass spectrometry imaging of plant tissues: towards a plant metabolite atlas. *Analyst* **140**: 7696–7709.
- Bianchi G, Figini ML. 1986. Epicuticular waxes of glaucous and nonglaucous durum wheat lines. *Journal of Agricultural and Food Chemistry* **34**: 429–433.
- Bino RJ, Hall RD, Fiehn O, Kopka J, Saito K, Draper J, Nikolau BJ, Mendes P, Roessner-Tunali U, Beale MH *et al.* 2004. Potential of metabolomics as a functional genomics tool. *Trends in Plant Science* **9**: 418–425.
- Bokhart MT, Nazari M, Garrard KP, Muddiman DC. 2018. MSIReader v1.0: evolving open-source mass spectrometry imaging software for targeted and untargeted analyses. *Journal of The American Society for Mass Spectrometry* **29**: 8–16.
- Burkhow SJ, Stephens NM, Mei Y, Dueñas ME, Freppon DJ, Ding G, Smith SC, Lee Y-J, Nikolau BJ, Whitham SA *et al.* 2018. Characterizing virus-induced gene silencing at the cellular level with in situ multimodal imaging. *Plant Methods* **14**: 1–12.
- Buschhaus C, Herz H, Jetter R. 2007. Chemical composition of the epicuticular and intracuticular wax layers on adaxial sides of *Rosa canina* leaves. *Annals of Botany* **100**: 1557–1564.
- Cárdenas PD, Sonawane PD, Heinig U, Jozwiak A, Panda S, Abebie B, Kazachkova Y, Pliner M, Unger T, Wolf D *et al.* 2019. Pathways to defense metabolites and evading fruit bitterness in genus *Solanum* evolved through 2-oxoglutarate-dependent dioxygenases. *Nature Communications* **10**: 5169.
- Costa JH, Bazioli JM, de Vilhena Araújo E, Vendramini PH, de Freitas Porto MC, Eberlin MN, Souza-Neto JA, Fill TP. 2019. Monitoring indole alkaloid production by *Penicillium digitatum* during infection process in citrus by Mass Spectrometry Imaging and molecular networking. *Fungal Biology* **123**: 594–600.
- Dong Y, Li B, Aharoni A. 2016a. More than pictures: when MS imaging meets histology. *Trends in Plant Science* **21**: 686–698.
- Dong Y, Li B, Malitsky S, Rogachev I, Aharoni A, Kaftan F, Svatoš A, Franceschi P. 2016b. Sample preparation for mass spectrometry imaging of plant tissues: a review. *Frontiers in Plant Science* **7**: 60.
- Dreisewerd K. 2003. The desorption process in MALDI. *Chemical Reviews* **103**: 395–426.
- Eigenbrode SD, Jetter R. 2002. Attachment to plant surface waxes by an insect predator. *Integrative and Comparative Biology* **42**: 1091–1099.
- Fantini E, Falcone G, Frusciantè S, Giliberto L, Giuliano G. 2013. Dissection of tomato lycopene biosynthesis through virus-induced gene silencing. *Plant Physiology* **163**: 986–998.
- Feldberg L, Dong Y, Heinig U, Rogachev I, Aharoni A. 2018. DLEMMA-MS-imaging for identification of spatially localized metabolites and metabolic network map reconstruction. *Analytical Chemistry* **90**: 10231–10238.
- Fernández V, Guzmán P, Peirce CAE, McBeath TM, Khayet M, McLaughlin MJ. 2014. Effect of wheat phosphorus status on leaf surface properties and permeability to foliar-applied phosphorus. *Plant and Soil* **384**: 7–20.

- Friedman M. 2013. Anticarcinogenic, cardioprotective, and other health benefits of tomato compounds lycopene, α -tomatine, and tomatidine in pure form and in fresh and processed tomatoes. *Journal of Agricultural and Food Chemistry* 61: 9534–9550.
- Fu T, Houël E, Amusant N, Touboul D, Genta-Jouve G, Della-Negra S, Fisher GL, Brunelle A, Duplais C. 2019. Biosynthetic investigation of γ -lactones in *Sextonia rubra* wood using in situ TOF-SIMS MS/MS imaging to localize and characterize biosynthetic intermediates. *Scientific Reports* 9: 951.
- Gandía-Herrero F, García-Carmona F. 2013. Biosynthesis of betalains: yellow and violet plant pigments. *Trends in Plant Science* 18: 334–343.
- Hen-Avivi S, Savin O, Racovita R, Lee W-S, Adamki N, Malitsky S, Almekias-Siegl E, Levy M, Vautrin S, Bergès H *et al.* 2016. A metabolic gene cluster in the wheat W1 and the barley Cer-cqu Loci determines β -diketone biosynthesis and glaucousness. *Plant Cell* 28: 1440–1460.
- Heyman HM, Dubery IA. 2016. The potential of mass spectrometry imaging in plant metabolomics: a review. *Phytochemistry Reviews* 15: 297–316.
- Horn PJ, Chapman KD. 2014a. Lipidomics *in situ*: insights into plant lipid metabolism from high resolution spatial maps of metabolites. *Progress in Lipid Research* 54: 32–52.
- Horn PJ, Chapman KD. 2014b. Metabolite Imager: customized spatial analysis of metabolite distributions in mass spectrometry imaging. *Metabolomics* 10: 337–348.
- Horn PJ, James CN, Gidda SK, Kilaru A, Dyer JM, Mullen RT, Ohlrogge JB, Chapman KD. 2013. Identification of a new class of lipid droplet-associated proteins in plants. *Plant Physiology* 162: 1926–1936.
- Huang D, Feurtado JA, Smith MA, Flatman LK, Koh C, Cutler AJ. 2017. Long noncoding miRNA gene represses wheat β -diketone waxes. *Proceedings of the National Academy of Sciences, USA* 114: E3149–E3158.
- Itkin M, Rogachev I, Alkan N, Rosenberg T, Malitsky S, Masini L, Meir S, Iijima Y, Aoki K, de Vos R *et al.* 2011. GLYCOALKALOID METABOLISM1 is required for steroidal alkaloid glycosylation and prevention of phytotoxicity in tomato. *Plant Cell* 23: 4507–4525.
- Jetter R, Schäffer S. 2001. Chemical composition of the *Prunus laurocerasus* leaf surface. Dynamic changes of the epicuticular wax film during leaf development. *Plant Physiology* 126: 1725–1737.
- Koornneef M, Alonso-Blanco C, Vreugdenhil D. 2004. Naturally occurring genetic variation in *Arabidopsis thaliana*. *Annual Review of Plant Biology* 55: 141–172.
- Korenblum E, Dong Y, Szymanski J, Panda S, Jozwiak A, Massalha H, Meir S, Rogachev I, Aharoni A. 2020. Rhizosphere microbiome mediates systemic root metabolite exudation by root-to-root signaling. *Proceedings of the National Academy of Sciences, USA* 117: 3874–3883.
- Li B, Dunham SJB, Dong Y, Yoon S, Zeng M, Sweedler JV. 2016. Analytical capabilities of mass spectrometry imaging and its potential applications in food science. *Trends in Food Science & Technology* 47: 50–63.
- Li D, Heiling S, Baldwin IT, Gaquerel E. 2016. Illuminating a plant's tissue-specific metabolic diversity using computational metabolomics and information theory. *Proceedings of the National Academy of Sciences, USA* 113: E7610–E7618.
- Manicke NE, Dill AL, Ifa DR, Cooks RG. 2010. High-resolution tissue imaging on an orbitrap mass spectrometer by desorption electrospray ionization mass spectrometry. *Journal of Mass Spectrometry* 45: 223–226.
- Matsuda F, Okazaki Y, Oikawa A, Kusano M, Nakabayashi R, Kikuchi J, Yonemaru JI, Ebana K, Yano M, Saito K. 2012. Dissection of genotype–phenotype associations in rice grains using metabolome quantitative trait loci analysis. *The Plant Journal* 70: 624–636.
- Mintz-Oron S, Mandel T, Rogachev I, Feldberg L, Lotan O, Yativ M, Wang Z, Jetter R, Venger I, Adato A *et al.* 2008. Gene expression and metabolism in tomato fruit surface tissues. *Plant Physiology* 147: 823–851.
- Moussaieff A, Rogachev I, Brodsky L, Malitsky S, Toal TW, Belcher H, Yativ M, Brady SM, Benfey PN, Aharoni A. 2013. High-resolution metabolic mapping of cell types in plant roots. *Proceedings of the National Academy of Sciences, USA* 110: E1232–E1241.
- Orzaez D, Medina A, Torre S, Fernandez-Moreno J-P, Rambla JL, Fernández-Del-Carmen A, Butelli E, Martin C, Granell A. 2009. A visual reporter system for virus-induced gene silencing in tomato fruit based on anthocyanin accumulation. *Plant Physiology* 150: 1122–1134.
- Ossipov V, Ossipova S, Bykov V, Oksanen E, Koricheva J, Haukioja E. 2007. Application of metabolomics to genotype and phenotype discrimination of birch trees grown in a long-term open-field experiment. *Metabolomics* 4: 39–51.
- Palmer A, Trede D, Alexandrov T. 2016. Where imaging mass spectrometry stands: here are the numbers. *Metabolomics* 12: 107.
- Polturak G, Aharoni A. 2018. ‘La Vie en Rose’: biosynthesis, sources, and applications of Betalain pigments. *Molecular Plant* 11: 7–22.
- Polturak G, Breitl D, Grossman N, Perdigon AS, Weithorn E, Pliner M, Orzaez D, Granell A, Rogachev I, Aharoni A. 2016. Elucidation of the first committed step in betalain biosynthesis enables the heterologous engineering of betalain pigments in plants. *New Phytologist* 210: 269–283.
- Polturak G, Grossman N, Vela-Corcía D, Dong Y, Nudel A, Pliner M, Levy M, Rogachev I, Aharoni A. 2017. Engineered gray mold resistance, antioxidant capacity, and pigmentation in betalain-producing crops and ornamentals. *Proceedings of the National Academy of Sciences, USA* 114: 9062–9067.
- Polturak G, Heinig U, Grossman N, Battat M, Leshkowitz D, Malitsky S, Rogachev I, Aharoni A. 2018. Transcriptome and metabolic profiling provides insights into Betalain biosynthesis and evolution in *Mirabilis jalapa*. *Molecular Plant* 11: 189–204.
- Putri SP, Nakayama Y, Matsuda F, Uchikata T, Kobayashi S, Matsubara A, Fukusaki E. 2013. Current metabolomics: Practical applications. *Journal of Bioscience and Bioengineering* 115: 579–589.
- Qin L, Zhang Y, Liu Y, He H, Han M, Li Y, Zeng M, Wang X. 2018. Recent advances in matrix-assisted laser desorption/ionisation mass spectrometry imaging (MALDI-MSI) for in situ analysis of endogenous molecules in plants. *Phytochemical Analysis* 29: 351–364.
- Racovita RC, Jetter R. 2016. Composition of the epicuticular waxes coating the adaxial side of *Phyllostachys aurea* leaves: identification of very-long-chain primary amides. *Phytochemistry* 130: 252–261.
- R Core Team. 2019. *R: A language and environment for statistical computing*. R Foundation for Statistical Computing, Vienna, Austria. [WWW document] URL <https://www.R-project.org/>
- Rong JK, Millet E, Manisterski J, Feldman M. 2000. A new powdery mildew resistance gene: Introgression from wild emmer into common wheat and RFLP-based mapping. *Euphytica* 115: 121–126.
- Saito K, Matsuda F. 2010. Metabolomics for functional genomics, systems biology, and biotechnology. *Annual Review of Plant Biology* 61: 463–489.
- Schleyer G, Shahaf N, Ziv C, Dong Y, Meoded RA, Helfrich EJM, Schatz D, Rosenwasser S, Rogachev I, Aharoni A *et al.* 2019. In plaque-mass spectrometry imaging of a bloom-forming alga during viral infection reveals a metabolic shift towards odd-chain fatty acid lipids. *Nature Microbiology* 4: 527–538.
- Schwachtje J, Kutschbach S, Baldwin IT. 2008. Reverse genetics in ecological research. *PLoS ONE* 3: e1543.
- Schwahn K, de Souza LP, Fernie AR, Tohge T. 2014. Metabolomics-assisted refinement of the pathways of steroidal glycoalkaloid biosynthesis in the tomato clade. *Journal of Integrative Plant Biology* 56: 864–875.
- Sonawane PD, Heinig U, Panda S, Gilboa NS, Yona M, Kumar SP, Alkan N, Unger T, Bocobza S, Pliner M *et al.* 2018. Short-chain dehydrogenase/reductase governs steroidal specialized metabolites structural diversity and toxicity in the genus *Solanum*. *Proceedings of the National Academy of Sciences, USA* 115: E5419–E5428.
- Sturtevant D, Lee YJ, Chapman KD. 2016. ScienceDirect Matrix assisted laser desorption/ionization-mass spectrometry imaging (MALDI-MSI) for direct visualization of plant metabolites in situ. *Current Opinion in Biotechnology* 37: 53–60.
- Sturtevant D, Lu S, Zhou ZW, Shen Y, Wang S, Song JM, Zhong J, Burks DJ, Yang ZQ, Yang QY *et al.* 2020. The genome of jojoba (*Simmondsia chinensis*): a taxonomically isolated species that directs wax ester accumulation in its seeds. *Science Advances* 6: eaay3240.
- Sumner LW, Lei Z, Nikolau BJ, Saito K. 2015. Modern plant metabolomics: advanced natural product gene discoveries, improved technologies, and future prospects. *Natural Product Reports* 32: 212–229.

- Sumner LW, Mendes P, Dixon RA. 2003. Plant metabolomics: large-scale phytochemistry in the functional genomics era. *Phytochemistry* 62: 817–836.
- Tanaka Y, Sasaki N, Ohmiya A. 2008. Biosynthesis of plant pigments: anthocyanins, betalains and carotenoids. *The Plant Journal* 54: 733–749.
- Tang Y, Horikoshi M, Journal WLTR. 2016. ggfortify: unified interface to visualize statistical results of popular R packages. *The R Journal* 8: 478–489.
- Tohge T, Fernie AR. 2010. Combining genetic diversity, informatics and metabolomics to facilitate annotation of plant gene function. *Nature Protocols* 5: 1210–1227.
- Vaghchhipawala Z, Rojas CM, Senthil-Kumar M, Mysore KS. 2011. Agroinoculation and agroinfiltration: simple tools for complex gene function analyses. In: Pereira A, ed. *Plant reverse genetics*. Totowa, NJ, USA: Humana Press, 65–76.
- Vanhercke T, El Tahchy A, Liu Q, Zhou XR, Shrestha P, Divi UK, Ral JP, Mansour MP, Nichols PD, James CN *et al.* 2014. Metabolic engineering of biomass for high energy density: oilseed-like triacylglycerol yields from plant leaves. *Plant Biotechnology Journal* 12: 231–239.
- Wang Jian, Wilhelmina Kalt A, Sporns Peter. 2000. Comparison between HPLC and MALDI-TOF MS Analysis of Anthocyanins in Highbush Blueberries. *Journal of Agricultural and Food Chemistry* 48: 3330–3335.
- Wickham H. 2016. *ggplot2: elegant graphics for data analysis*. New York, NY, USA: Springer.
- Wroblewski T, Tomczak A, Micheltore R. 2005. Optimization of Agrobacterium-mediated transient assays of gene expression in lettuce, tomato and Arabidopsis. *Plant Biotechnology Journal* 3: 259–273.
- Yamanaka T, Vincken JP, Zuilhof H, Legger A, Takada N, Gruppen H. 2009. C22 Isomerization in α -tomatine-to-esculeoside a conversion during tomato ripening is driven by C27 hydroxylation of triterpenoidal skeleton. *Journal of Agricultural and Food Chemistry* 57: 3786–3791.
- Zampieri M, Sauer U. 2017. Metabolomics-driven understanding of genotype-phenotype relations in model organisms. *Current Opinion in Systems Biology* 6: 28–36.
- Zhang Z, Wang W, Li W. 2013. Genetic interactions underlying the biosynthesis and inhibition of β -diketones in wheat and their impact on glucosinoid and cuticle permeability. *PLoS ONE* 8: e54129.

Supporting Information

Additional Supporting Information may be found online in the Supporting Information section at the end of the article.

Fig. S1 Overview of a typical MALDI imaging workflow.

Fig. S2 Comparison of *GAME25* expression between *GAME25*-RNAi transgenic tomato lines and wild-type tomato fruits at mature green (MG) and mature red (MR) stages using quantitative real time-PCR assay.

Fig. S3 Score plots of principal component analysis of metabolic profiles showed clear discrimination between *GAME25*-RNAi transgenic tomato lines and wild-type tomato fruits at mature green and mature red stages.

Fig. S4 Score plot of principal component analysis of metabolic profiles showed that nonsilenced sectors from control and *GAME31*-VIGS tomato fruits were clustered together, while

VIGS-silenced sectors from control and *GAME31*-VIGS tomato fruits were clearly separated.

Fig. S5 Localisation and quantitative comparison of steroidal glycoalkaloids (SGAs) in *GAME31*-VIGS tomato fruits at mature red ripe stage.

Fig. S6 Direct MALDI imaging of betalains from PX11 expressing *N. benthamiana* leaves following agroinfiltration.

Fig. S7 Comparison of the spatial distribution of *m/z* 303.049 from *GAME31*-VIGS, Control and wild-type tomato fruits.

Methods S1 MALDI imaging, LC-MS analysis of steroidal glycoalkaloids, anthocyanins and betalains, GC-MS analysis of epicuticular wax, and quantitative real-time PCR analysis.

Table S1 Putative steroidal glycoalkaloids identified in *GAM25i* and wild-type tomato fruit using LC-MS analysis.

Table S2 Putative steroidal glycoalkaloids identified in *GAM25i* and wild-type tomato fruit using MALDI.

Table S3 Putative anthocyanins identified in *GAME31*-VIGS and control tomato fruit using LC-MS analysis.

Table S4 Putative anthocyanins identified in *GAME31*-VIGS and control tomato fruit using MALDI.

Table S5 Putative betalains identified in PX11- and PX13-expressing *N. benthamiana* leaves following agroinfiltration using MALDI.

Table S6 Putative betalains identified in PX11 and PX13 expressing *N. benthamiana* leaves following agroinfiltration using LC-MS analysis.

Table S7 Putative epicuticular waxes identified in BL and 2BS**CASL* flag leaves using GC-MS analysis.

Table S8 Putative epicuticular waxes identified in BL and 2BS**CASL* flag leaves using MALDI.

Please note: Wiley Blackwell are not responsible for the content or functionality of any Supporting Information supplied by the authors. Any queries (other than missing material) should be directed to the *New Phytologist* Central Office.